Mon. Not. R. Astron. Soc. **336,** 932–944 (2002)

RXTE observations of 3C 273 between 1996 and 2000: variability time-scale and jet power

Jun Kataoka,[1,2]★ Chiharu Tanihata,[3,4] Nobuyuki Kawai,[1,2] Fumio Takahara,[5] Tadayuki Takahashi,[3,4] Philip G. Edwards[3] and Fumiyoshi Makino[2]

[1]*Department of Physics, Faculty of Science, Tokyo Institute of Technology, Meguro-ku, Tokyo, Japan*
[2]*National Space Agency of Japan, Tsukuba, Ibaragi, Japan*
[3]*Institute of Space and Astronautical Science, Sagamihara, Kanagawa, Japan*
[4]*Department of Physics, Faculty of Science, University of Tokyo, Tokyo, Japan*
[5]*Department of Earth and Space Science, Toyonaka, Osaka, Japan*

Accepted 2002 July 1. Received 2002 May 27; in original form 2002 February 4

ABSTRACT

We present the results of a long-look monitoring of 3C 273 with *RXTE* between 1996 and 2000. A total of 230 observations amounts to a net exposure of 845 ks, with this spectral and variability analysis of 3C 273 covering the longest observation period available at hard X-ray energies. Flux variations by a factor of 4 have been detected over 4 yr, whereas flux variations of less than 30 per cent have been observed for individual flares on time-scales of ∼3 d. Two temporal methods, the power spectrum density (PSD) and the structure function (SF), have been used to study the variability characteristics of 3C 273. The hard X-ray photon spectra generally show a power-law shape with a differential photon index of $\Gamma \simeq 1.6 \pm 0.1$. In 10 of 261 data segments, exceptions to power-law behaviour have been found: (i) an additional soft excess below 4 keV; and (ii) a broad Fe fluorescent line feature with EW ∼ 100–200 eV. Our new observations of these previously reported X-ray features may imply that 3C 273 is a unique object whose hard X-ray emission occasionally contains a component that is not related to a beamed emission (Seyfert-like), but most hard X-rays are likely to originate in inverse Compton radiation from the relativistic jet (blazar-like). Multifrequency spectra from radio to γ-rays are presented in addition to our *RXTE* results. The X-ray time variability and spectral evolution are discussed in the framework of the beamed, synchrotron self-Compton picture. We consider the 'power balance' (both radiative and kinetic) between the accretion disc, the sub-parsec-scale jet and the 10-kpc-scale jet.

Key words: radiation mechanisms: non-thermal – quasars: individual: 3C 273 – X-rays: galaxies.

1 INTRODUCTION

As the brightest and nearest ($z = 0.158$) quasar, 3C 273 is the ideal laboratory for studying active galactic nuclei (AGN). Studies of this source are relevant to all AGN physics, as 3C 273 displays significant flux variations, has a well-measured wide-band spectral energy distribution, and has a relativistic jet originating in its central core (see Courvoisier 1998 for a review). Very long baseline interferometry (VLBI) radio observations of the parsec-scale jet have shown a number of jet components moving away from the core at velocities apparently faster than the speed of light (e.g. Pearson et al. 1981; Vermeulen & Cohen 1994). The collimated jet structure extends up to ∼50 kpc from the core. Since 3C 273 is bright at all wavelengths and on various scalesizes, it provides a valuable opportunity to probe the most inner part of the accretion disc (∼10^{-4} pc) as well as the large-scale jet (∼10^4 pc) at the same time.

3C 273 is generally classified as a blazar and is also a prominent γ-ray source. It was the only extragalactic source of γ-rays identified in *COS-B* observations (Swanenburg et al. 1978), and was subsequently detected at energies in the 0.05–10 MeV range with OSSE (McNaron-Brown et al. 1995), in the 0.75–30 MeV range with COMPTEL (Schönfelder et al. 2000), and above 100 MeV in numerous EGRET observations (Hartman et al. 1999). EGRET observations helped to establish that the overall spectra of blazars (plotted as νF_ν) have two pronounced continuum components: one peaking between infrared and X-rays, and the other in the γ-ray regime (e.g. Mukherjee et al. 1997). The low-energy component is

★E-mail: kataoka@hp.phys.titech.ac.jp

believed to be produced by synchrotron radiation from relativistic electrons in magnetic fields, while inverse Compton scattering by the same electrons is thought to be the dominant process responsible for the high-energy γ-ray emission (Ulrich, Maraschi & Urry 1997). The radiation is emitted from a relativistic jet, directed close to our line of sight (e.g. Urry & Padovani 1995).

3C 273 is no exception to this picture, but an additional 'big blue bump' (hereafter BBB) dominates the optical–soft-X-ray emission [see Paltani, Courvoisier & Walter (1998) and Robson (1996) for a review]. Interestingly, although similar excesses have been observed in the optical–ultraviolet region of Seyfert galaxies, they have not been reported for any blazar other than 3C 273. Although its origin is still far from being understood, it has been proposed that the BBB may be due to thermal emission from the surface of a standard accretion disc (Shields 1978), including optically thin parts of the disc and a corona (see Czerny 1994 for a review). Various models have been suggested (e.g. Courvoisier & Clavel 1991), but it is generally agreed that the BBB is nearly isotropic emission from the vicinity of the central black hole, presumably from the accretion disc.

The presence of a fluorescent emission line at 6.4 keV is a signature of X-ray reprocessing by cold material. There is some evidence for the presence of a weak line at this energy in the X-ray spectrum of 3C 273. One of the *Ginga* observations showed evidence for the line at 99 per cent level, but the other observations provided only upper limits (Turner et al. 1990). A line detection is also reported by Grandi et al. (1997) and Haardt et al. (1998) in a *BeppoSAX* observation in 1996. *ASCA* provided only upper limits in a 1993 observation (Yaqoob et al. 1994), whereas a broad-line feature was clearly detected in 1996 observations. This somewhat confused situation probably means that both thermal (as for Seyferts) and non-thermal (as for blazars) emission processes are taking place in this particular object. However, it is completely unknown (i) which process dominates the radiation and (ii) how often the Fe line is 'visible' in the photon spectrum.

Many γ-ray blazars, including 3C 273, have shown large flux variations, on time-scales as short as a day for some objects (e.g. von Montigny et al. 1997; Mukherjee et al. 1997). However, there are only a few blazars with variability characteristics that are well studied in the high-energy bands (both X-ray and γ-ray bands). For example, recent X-ray studies of Mrk 421, the prototypical 'TeV-emitting' blazar, have revealed that (i) the variability time-scale is $\sim$1 d, and (ii) the flux variation in the X-ray and the TeV γ-ray bands is well correlated on time-scales of a day to years (see Takahashi et al. 2000; Kataoka et al. 2001). Clearly, these observations provide important clues to understanding jet physics, and potentially for discriminating between various emission models for blazars. Although 3C 273 is a bright object and particularly well-sampled, it has not yet been possible to undertake such studies since data from previous X-ray satellites were too sparse (e.g. the 13 observations spanning over 5 years of Turner et al. 1990).

In this paper, we analyse the archival hard X-ray data obtained with *RXTE* between 1996 and 2000, with a total exposure of 845 ks. This report of both the temporal and spectral variability of 3C 273 is thus based on the highest quality and most densely sampled data in this energy band. The observation and data reduction are described in Section 2. Two temporal methods are introduced: the power spectrum density (Section 3.1) and the structure function (Section 3.2). The X-ray spectral evolutions are summarized in Sections 4.1 and 4.2. Multifrequency spectra are presented in Section 4.3. In Section 5, we discuss scenarios that systematically account for the hard X-ray variability and spectral evolution of 3C 273. Throughout the paper, we discuss the energetics between the central engine and the relativistic jet, taking into account observations of the large-scale jet by *Einstein*, *ROSAT* and *Chandra*. Finally, in Section 6, we present our conclusions.

Throughout this paper, we adopt $H_0 = 75\ \mathrm{km\ s^{-1}\ Mpc^{-1}}$ and $q_0 = 0.5$. The luminosity distance to the source is $d_\mathrm{L} = 2.02 \times 10^{27}$ cm.

2 OBSERVATIONS AND DATA REDUCTION

3C 273 was observed 230 times with the X-ray satellite *RXTE* between 1996 February and 2000 February, with a net exposure of 845 ks. The observations are summarized in Table 1. All *RXTE* observations were performed with Good Xe-16s plus Standard 1/2 modes for the Proportional Counter Array (PCA: Jahoda et al. 1996). The source counts were extracted from three Proportional Counter Units (PCU0/1/2) for the 1996–99 observations, which had much larger and less interrupted exposures than those for PCU3 and PCU4. After 1999 May, PCU1 experienced the same 'discharge problems' as for PCU3 and PCU4, and was often operated with a reduced high-voltage supply. We thus use the data from two PCUs (PCU0/2) for the analysis of 1999 May to 2000 February observations (119 ks of P40176).

We used only signals from the top layer (X1L and X1R) in order to obtain the best signal-to-noise ratio. Standard screening procedures were performed on the data, using the analysis software package HEASOFT 5.0 provided by NASA/Goddard Space Flight Center. Backgrounds were estimated using PCABACKEST (version 2.1b) for the PCA, and subtracted from the data. We have not used data from the High Energy X-ray Timing Experiment (HEXTE) on board *RXTE*, for two reason: (i) the typical exposure for *RXTE*

Table 1. Observation log of 3C 273.

Obs. ID	Obs. date	Obs. times[a]	Exposure (ks)	Data mode[b]
P10330[c]	1996 Jul 16 23:15–1996 Jul 18 13:21	6	116.6	S1/S2/GX1/GX2
P10354	1996 Feb 02 01:12–1996 Aug 24 01:30	28	23.7	S1/S2/GX1/GX2
P20349	1996 Nov 03 15:30–1997 Dec 23 22:57	132	133.7	S1/S2/GX1/GX2
P30805	1998 Jun 24 07:44–1998 Jun 26 09:05	3	33.2	S1/S2/GX1/GX2
P40176	1999 Jan 04 06:25–2000 Feb 24 09:24	57	473.3	S1/S2/GX1/GX2
P40177	1999 Jan 19 18:32–1999 Feb 01 20:15	4	64.6	S1/S2/GX1/GX2
total		230	845.1	

[a] Number of observations conducted for each proposal.
[b] S1: Standard 1; S2: Standard 2; GX1: Good Xe-1 16s; GX2: Good Xe-2 16s.
[c] Four observations with large offset angle ($\geqslant 0\overset{\circ}{.}5$) were not used for the analysis.

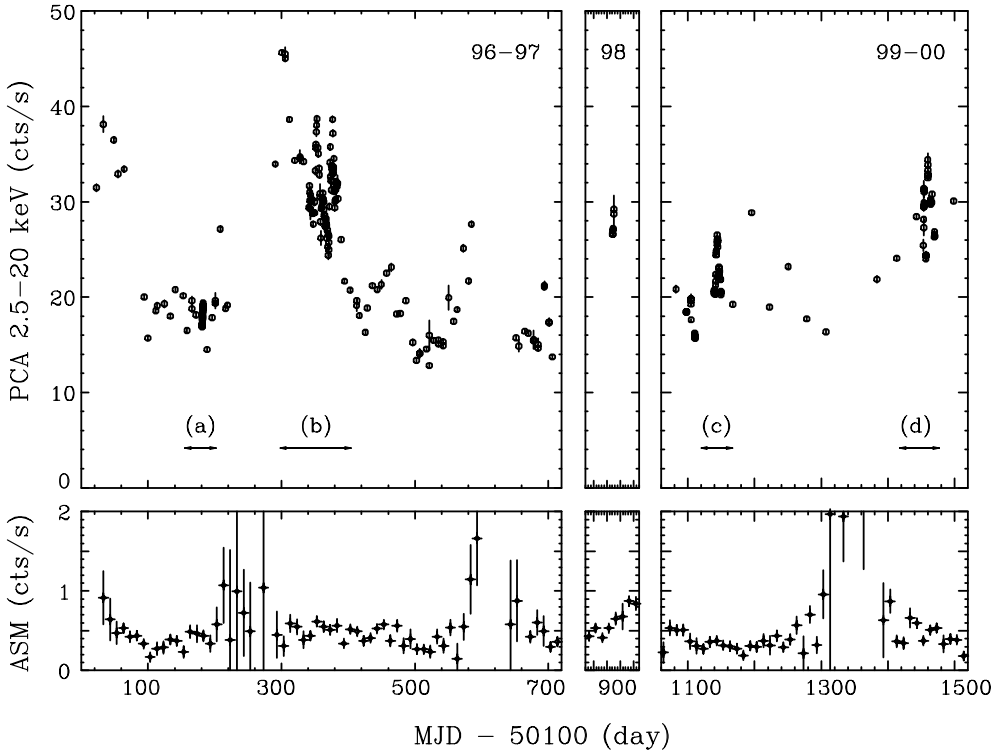

Figure 1. Upper panel: long-term light curve of 3C 273. The count rates of the top layer from *RXTE* PCU0/2 detectors are summed in the 2.5–20 keV energy range. Lower panel: the count rates of the ASM on board *RXTE*. The data are binned in 10-d intervals.

observations was too short to yield meaningful hard X-ray data for this variable source above 20 keV; and (ii) calibration problems make the analysis results quite uncertain. Similar problems exist for the All Sky Monitor (ASM) data on board *RXTE*. Given the large systematic errors already known (e.g. enhanced noise at certain solar angles) in ASM faint source data, we cannot justify the use of ASM data for detailed temporal studies.

In order to obtain the maximum photon statistics and the best signal-to-noise ratio, we selected the energy range 2.5–20 keV for the PCA. The overall light curves are shown in Fig. 1. The ASM light curve (2–10 keV rates), in 10-d bins, is shown for comparison with the PCA flux variations (although one finds no clear correlation between them, because of the ASM problems described above). We have used a bin size of 5760 s (approximately the *RXTE* orbital period) for the PCA plot. The 2PCU (PCU0/2) count rates are plotted for all data from 1996 to 2000. Expanded plots of the segments (a)–(d), indicated by arrows in Fig. 1, are shown in Fig. 2. An intensive hard X-ray monitoring for more than a month was conducted in 1996 simultaneously with infrared telescopes [segment (b) in Figs 1 and 2]. Results from this campaign have been discussed by M^{c}Hardy et al. (1999).

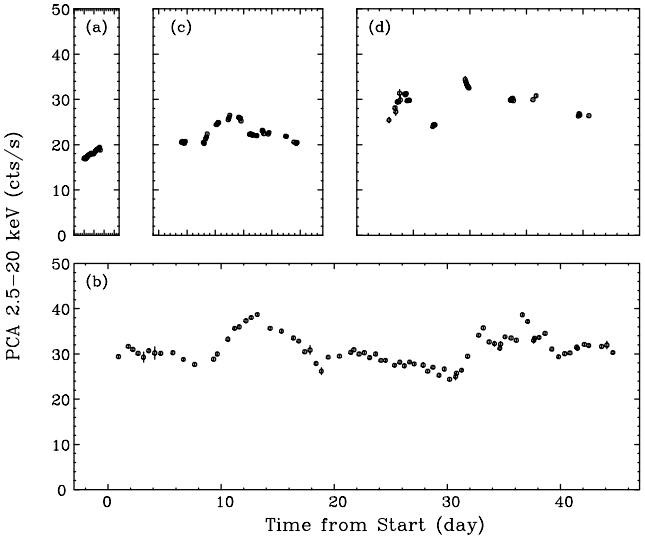

Figure 2. Expanded plots of Fig. 1. The light curves are separately given for (a)–(d). The scale of the time axis is same in all plots.

3 TEMPORAL STUDY

3.1 Power spectrum density

A power spectrum density (PSD) analysis is most commonly used to characterize the source variability. The *RXTE* data presented in this paper are the highest quality data ever reported in the X-ray band, enabling us to determine the PSD over a wider frequency range than attempted previously. An important issue, however, is the data gaps, which are unavoidable for low-orbit X-ray satellites. Moreover, we must take great care since the observations were sparsely scheduled; a net exposure of 845 ks corresponds to only 0.7 per cent of the total span of 4 yr. In order to reduce the effect of data sampling, we follow a technique for calculating the PSD of unevenly sampled light curves (e.g. Hayashida et al. 1998).

The *normalized* PSD (NPSD) at frequency f is defined as

$$P(f) = \frac{\left[a^2(f) + b^2(f) - \sigma^2_{\rm stat}/n\right]T}{F^2_{\rm av}},$$
$$a(f) = \frac{1}{n}\sum_{j=0}^{n-1} F_j \cos(2\pi f t_j), \quad (1)$$
$$b(f) = \frac{1}{n}\sum_{j=0}^{n-1} F_j \sin(2\pi f t_j),$$

where F_j is the source count rate at time t_j ($0 \leqslant j \leqslant n-1$), T is the data length of the time series, and $F_{\rm av}$ is the mean value of the source counting rate. The power arising from photon-counting statistics is given by $\sigma^2_{\rm stat}$.

To calculate the NPSD of our data sets, we made light curves of three different bin sizes for *RXTE* data (256, 5760 and 43 200 s). We then divided each light curve into 'segments', which are defined as continuous parts of the light curve. If the light curve contains a time-gap larger than twice the bin size, we cut the light curve into two segments, one on each side of the gap. We then calculated the power at frequencies $f = k/T$ ($1 \leqslant k \leqslant n/2$) for each segment and took their average. The lowest frequency end ($\sim 10^{-6}$ Hz) is about half the inverse of the longest continuous segments, which is determined by the data in Fig. 2(b) in our case.

Fig. 3 shows the NPSD calculated using this procedure. These NPSD data are binned in logarithmic intervals of $\sim$0.2 (i.e. factors of approximately 1.6, as dictated by the data) to reduce the noise. The error bars represent the standard deviation of the average power in each rebinned frequency interval. The expected noise power arising from counting statistics, $\sigma^2_{\rm stat} T/nF^2_{\rm av}$, is shown in Fig. 3 as a dashed line. As the NPSD has a very steep power-law slope, with the NPSD decreasing as frequency increases, *no* detectable variability exists in the light curve for $f \geqslant 10^{-4}$ Hz (i.e. consistent with zero power for short-time-scale variability $\leqslant 10^4$ s).

A single-power-law function is *not* a good representation of the NPSD, as the power-law fit above 10^{-5} Hz is too steep for the data below 10^{-5} Hz [$\chi^2 = 14.7$ for eight d.o.f.; $P(\chi^2) = 6$ per cent]. A better fit was obtained using a broken power-law function, where the spectrum is harder below the break. The fitting function used was $P(f) \propto f^{-\alpha_{\rm L}}$ for $f \leqslant f_{\rm br}$ and $P(f) \propto f^{-\alpha}$ for $f \geqslant f_{\rm br}$. The goodness of the fit was significantly improved: $\chi^2 = 7.3$ for six d.o.f., $P(\chi^2) = 30$ per cent. The best-fitting parameters are $\alpha_{\rm L} = 1.4 \pm 0.2$, $\alpha = 2.6 \pm 0.1$ and $f_{\rm br} = (4.7 \pm 1.5) \times 10^{-6}$ Hz, respectively. This corresponds to a variability time-scale for individual flares of $t_{\rm var} \sim$ 3 d, as can be seen in Fig. 2.

3.2 Structure function

The structure function (hereafter SF) is a numerical technique similar to the traditional PSD, but which has some advantages for dealing with highly undersampled data. Since the SF is less affected by data gaps in light curves (e.g. Hughes, Aller & Aller 1992), it may be a useful estimator for our study. The definitions of SFs and their properties are given by Simonetti, Cordes & Heeschen (1985). The first-order SF is defined as

$$\mathrm{SF}(\tau) = \frac{1}{N}\sum [a(t) - a(t+\tau)]^2, \quad (2)$$

where $a(t)$ is a point in the time series (light curve) a, and the summation is made over all pairs separated in time by τ. The term N is the number of such pairs.

The SF is closely related to the PSD. If the structure function has a power-law form, $\mathrm{SF}(\tau) \propto \tau^{\beta}$ ($\beta \geqslant 0$), then the power spectrum has a distribution $P(f) \propto f^{-\alpha}$, where f is the frequency and $\alpha \simeq \beta + 1$. Obviously such an approximate relation is violated when β is close to zero, since both α and β approach zero for white noise. Nevertheless, the SF gives a crude but convenient estimate of the corresponding PSD distribution especially for red-noise-type PSDs (e.g. Paltani et al. 1997; Cagnoni, Papadakis & Fruscione 2001).

In Fig. 4, the SF is calculated from the light curve presented in Fig. 1. We used all the data as a 'continuous' observation in order to probe the variability on time-scales as long as possible. *RXTE* (PCA) light curves binned in 5760-s intervals were used for the calculation. The resulting SFs were normalized by the square of the mean fluxes and were binned at logarithmically equal intervals. The measurement noise (Poisson errors associated with flux uncertainty)

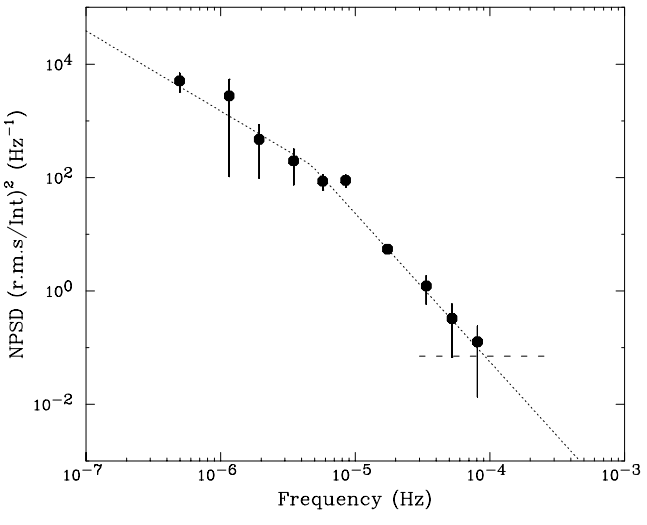

Figure 3. Normalized PSD (NPSD) calculated from the light curves in Fig. 1. The dotted line shows the best-fitting broken power-law function. Full details are given in the text.

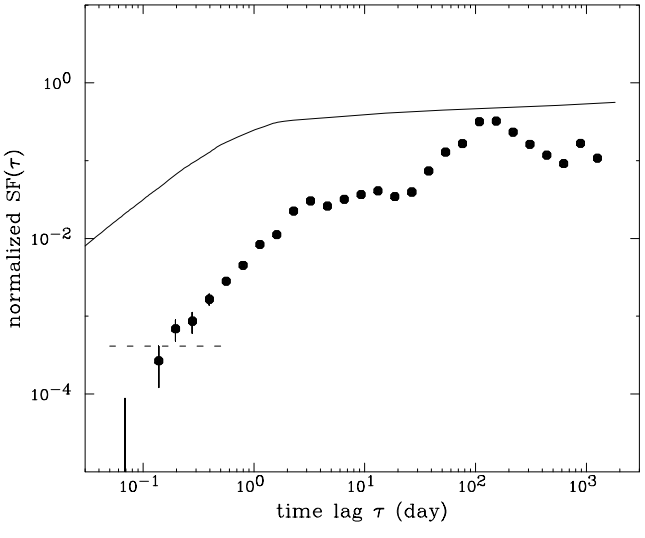

Figure 4. The SF calculated from the light curves of Fig. 1. The solid line shows the SF of Mrk 421 to compare with 3C 273. Full details are given in the text.

was subtracted as twice the square of Poisson errors on the fluxes (and the noise level is given as the dashed line in the figure).

As suggested by the NPSD in Fig. 3, the resulting SFs are characterized by a steep increase ($\beta \simeq 1.5$) in the time region of $0.1 \leqslant \tau \leqslant 3$ d, above which the SFs show a significant roll-over ($\beta \simeq 0.3$). A gradual rise continues up to a time lag of $\tau \sim 30$ d, where a significant 'bump' appears. This bump, and the 'wiggling' features at the longest time-scales may be artefacts caused by the sparse sampling of the light curve [see Cagnoni, Papadakis & Fruscione (2001) and Kataoka et al. (2001) for a detailed discussion]. The number of pairs [N in equation (2)] decreases as the time separation τ increases and, accordingly, the uncertainty becomes larger.

The most rigorous study of the nature of this 'bump' would be obtained by simulating the light curves characterized by a certain SF, and filtering them with the same window as the actual observation. The resulting SF could then be compared with that adopted for the simulations. However, such an estimate is only possible when we already know the *true* 'bump' structures of the system. The study of such structures is of interest in the light of claims for quasi-periodic oscillation (QPO) on time-scales of ∼100 d for other blazars (e.g. Rieger & Mannheim 2000; Abraham 2000), but is beyond the scope of this paper. Here we limit discussion of the SF to time-scales shorter than 10 d, where N (see equation 2) is large and the PSD and SF show good agreement.

In Fig. 4, we also show the SF of Mrk 421 calculated from *ASCA* observations over 5 yr for comparison (solid line; reproduced from Kataoka et al. 2001). Mrk 421 is an 'orthodox' blazar, and the best-studied blazar in the X-ray band. Two important characteristics are seen in the figure: (i) the structure functions of both Mrk 421 and 3C 273 show a roll-over at $1 \leqslant t_{\rm var} \leqslant 10$ d; and (ii) the normalized SF, which is proportional to the square of the variability amplitude, is 1–2 orders of magnitude *smaller* for 3C 273 than for Mrk 421.

4 SPECTRAL STUDY

4.1 X-ray spectral evolution: power-law component

Time variability of blazars is generally accompanied by significant spectral changes, which provide direct information about the acceleration, cooling and injection of electrons in the relativistic jet. Notably, such spectral information gives independent and/or alternative information to the variability studies presented in Section 3. In this section, we investigate the photon spectrum evolution of 3C 273 for each observation conducted from 1996 to 2000. We first divided the total exposure into one-orbit (5760 s) intervals to investigate the most rapid evolution in photon spectra as possible. Spectral fits have been performed individually for 261 segments over the 4 years of observations. A single-power-law function and a photoelectric absorbing column $N_{\rm H}$ fixed at the Galactic value (1.79×10^{20} cm^{-2}: Dickey & Lockman 1990) represent most of the spectra well in the 2.5–20 keV data. The reduced χ^2 for 251 segments (out of 261) ranges from 0.4 to 1.4 for 45 d.o.f., which corresponds to $P(\chi^2) \geqslant 5$ per cent.

We summarize the results of power-law fitting in Fig. 5. The upper panel shows the changes in the 2–10 keV flux and the evolution of the differential photon index (Γ) determined in the 2.5–20 keV band. We are aware that *RXTE* is not sensitive to photons in the 2.0–2.5 keV band. Nevertheless, the 2–10 keV flux is specifically selected because most previous works have defined the X-ray flux in this energy band (e.g. Turner et al. 1990; Yaqoob et al. 1994; Haardt et al. 1998). The 2–10 keV flux changes dramatically during the observations in 1996–2000: from 2.25×10^{-10} erg cm^{-2} s^{-1} at the brightest (MJD 50400.8) to 0.62×10^{-10} erg cm^{-2} s^{-1} at the faintest (MJD 50621.7). During the 1996–97 season, the hard X-ray spectral photon indices stayed almost constant, with a differential

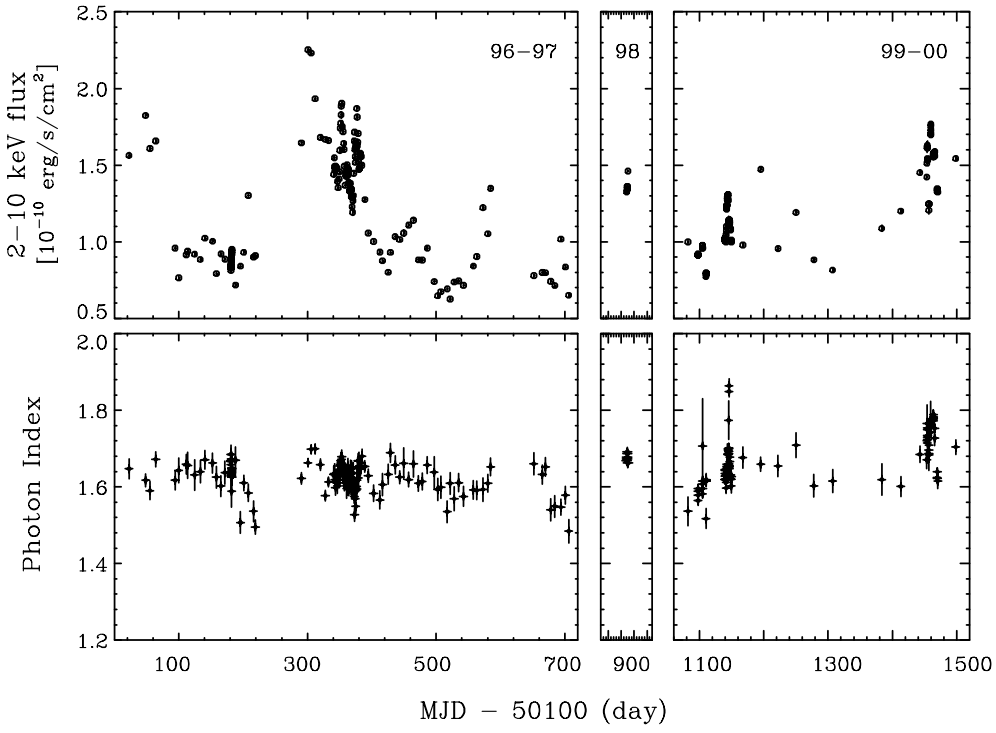

Figure 5. The spectral evolution of 3C 273 as a function of time. Upper panel: changes in the 2–10 keV flux. Lower: changes in the differential photon index Γ.

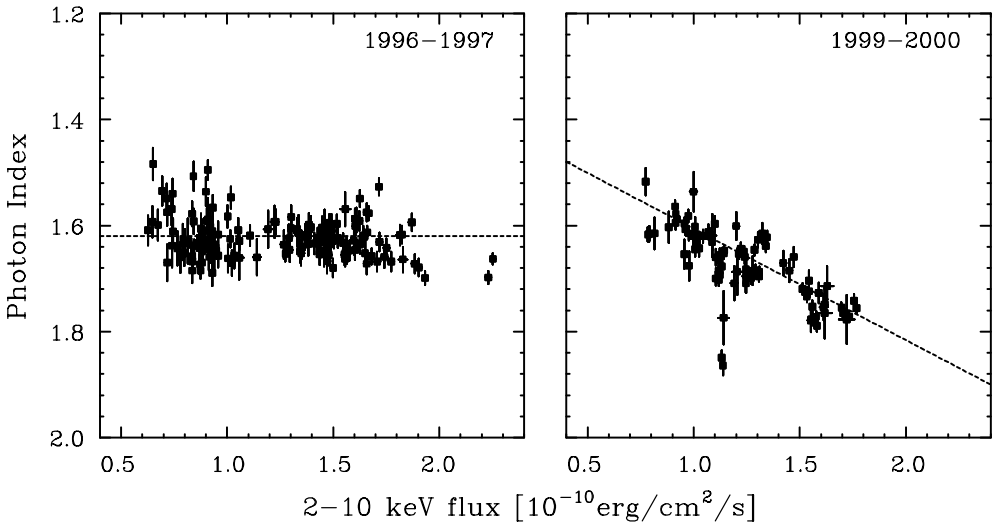

Figure 6. Correlations between the 2–10 keV flux and the photon index Γ. Left: those for the 1996–97 season (P10330, P10354, P20349); right: those for the 1999–2000 season (P40176, P40177).

photon index of $\Gamma = 1.6 \pm 0.1$. Larger spectral variation is seen in the 1999–2000 season, where Γ varies from 1.5 to 1.9.

The spectral evolution is more clearly seen in Fig. 6 where the correlations between the fluxes and the photon indices are separately plotted for the 1996–97 and 1999–2000 seasons. For the 1996–97 observations, the spectral shapes do not change significantly ($\Gamma \simeq 1.6$) despite large flux variations. The correlation factor between the flux and photon index is $R_{F\Gamma} = -0.19$. A stronger correlation has been found for 1999–2000 observations, where the spectral index becomes *softer* when the source is brighter ($R_{F\Gamma} = -0.73$).

4.2 The soft excess and broad-line feature

As mentioned above, 10 out of the 261 photon spectra cannot be fitted by a simple power-law function, in the sense that $P(\chi^2) \leqslant 5$ per cent. There are two different types of departure from a power-law spectrum: (i) a significant soft excess below 4 keV; and (ii) a broad-line feature seen at 5–6 keV (in the observer's frame).

Fig. 7 shows examples of νF_ν photon spectra for each case. The left-hand panel shows a concave feature with an apparent break at 4 keV [case (i)]. A simple power-law fitting to the data gives $\chi^2 = 1.4$ for 44 d.o.f., where $P(\chi^2) = 4$ per cent. Spectral fits with a broken power-law model significantly improve the goodness of the fit, as summarized in Table 2. Note that, below this break energy, the photon spectrum shows a very steep power-law index of $\Gamma_L = 2.27 \pm 0.19$. A similar soft excess has been found in the photon spectra of the segment closest in time (MJD 51246.15–51246.16); however, the statistical significance is relatively low and the simple power-law function gives a 'good' fit [$P(\chi^2) \geqslant 27$ per cent].

The broad-line features, as illustrated in Fig. 7 (right-hand panel), are observed nine times during the 1996–98 observations. The results of spectral fits to a power law plus Gaussian line model are given in Table 3. The line centre energy is distributed between 5.8 and 7.1 keV in the rest frame of the quasar. We cannot determine the exact shape and width of this broad line because of the limited sensitivity of the PCA on board *RXTE*. Following Yaqoob & Serlemitsos (2000), we thus fixed the intrinsic linewidth at $\sigma_{Fe} = 0.8$ keV. The equivalent width of the line ranges from 108 to 210 eV, although uncertainties are large. Taking these uncertainties into account, it seems premature to identify this structure as a broad Fe Kα line only using the *RXTE* data. Comparison with previous data, especially taken by instruments on board other satellites, is necessary for confirmation.

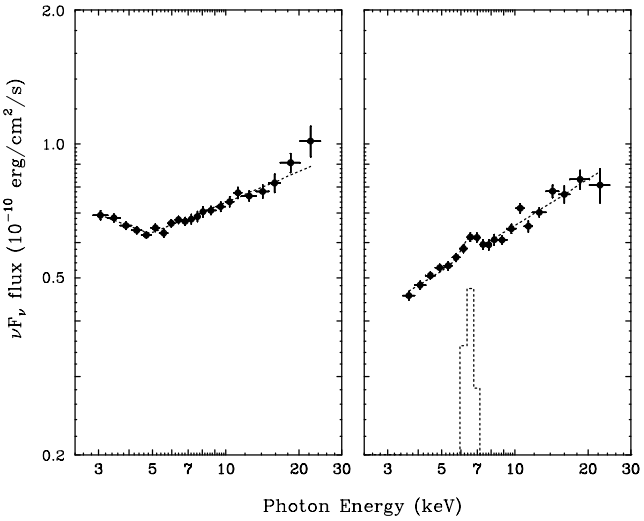

Figure 7. Examples of spectral fits to 3C 273 photon spectra when (a) a soft excess and (b) a broad-line feature are present. The spectra are from data segments MJD 51246.10–51246.12 and 50282.14–50282.17, respectively.

The broad-line feature was first reported by Turner et al. (1990) using the data taken by *EXOSAT* and *Ginga*. *RXTE* detections of the Fe Kα line from 3C 273 have been reported by Yaqoob & Serlemitsos (2000) for the observations on 1996 July 17–18 (MJD 50181–50182) and 1998 June 24–26 (MJD 50988–50990). Importantly, these observations were conducted simultaneously with *ASCA*. *ASCA* carried two different types of spectrometers, the Solid-state Imaging Spectrometer (SIS: Yamashita et al. 1997) and the Gas Imaging Spectrometer (GIS: Ohashi et al. 1996), both of which have much better line sensitivity than the *RXTE* PCA below 10 keV. Their results clearly indicate the existence of a broad-line feature around 6 keV of EW ∼ 100 eV (fig. 2 in Yaqoob & Serlemitsos (2000). Our analysis thus confirms the existence of broad-line features for two

Table 2. Spectral fits to 3C 273 with a broken power-law function.

Obs. date (MJD)	$\Gamma_{\rm L}^{a}$	$E_{\rm brk}^{b}$ (keV)	$\Gamma_{\rm H}^{c}$	2–10 keV flux (10^{-10} erg cm^2 s^{-1})	Reduced χ^2 (dof)	$\Delta\chi^{2d}$
51246.10–12	2.27 ± 0.19	4.02 ± 0.37	1.79 ± 0.02	1.17	0.86(42)	25.0

[a] Photon index of the low-energy power-law component.
[b] The break energy.
[c] Photon index of the high-energy power-law component.
[d] The decrease in χ^2 when the break is added to the simple power-law function.

Table 3. Spectral fits to 3C 273 with a power-law function plus Gaussian line model.

Obs. date (MJD)	Γ^{a}	$E_{\rm Fe}^{b}$ (keV)	$I_{\rm Fe}^{c}$ (10^{-4} cm^{-2} s^{-1})	EW^{d} (eV)	2–10 keV flux (10^{-10} erg cm^{-2} s^{-1})	χ^2 (d.o.f.)	$\Delta\chi^{2e}$
50281.14–17	1.63 ± 0.01	6.32 ± 0.19	2.40 ± 0.88	187 ± 68	0.82	0.75(43)	30.8
50282.01–05	1.62 ± 0.01	5.82 ± 0.17	2.91 ± 0.98	184 ± 62	0.88	0.78(43)	37.5
50282.14–17	1.65 ± 0.02	6.10 ± 0.30	1.65 ± 1.02	108 ± 67	0.91	1.18(42)	11.7
50282.28–31	1.62 ± 0.01	6.24 ± 0.20	2.44 ± 0.90	167 ± 62	0.92	0.85(43)	30.3
50282.35–38	1.65 ± 0.02	6.43 ± 0.19	2.87 ± 1.02	206 ± 73	0.92	1.21(43)	32.1
50300.90–91	1.62 ± 0.02	7.11 ± 0.27	2.53 ± 1.23	210 ± 102	0.93	1.02(30[f])	16.5
50400.82–83	1.65 ± 0.01	6.05 ± 0.23	4.98 ± 2.17	132 ± 58	2.24	1.04(43)	21.4
50454.33–34	1.63 ± 0.02	6.08 ± 0.26	5.44 ± 2.65	189 ± 92	1.74	1.09(43)	16.8
50988.32–36	1.65 ± 0.01	6.10 ± 0.21	2.54 ± 1.04	117 ± 48	1.31	1.09(43)	25.5

[a] Photon index of a power-law component.
[b] Line centre energy. Intrinsic linewidth is fixed at 0.8 keV.
[c] Intensity of a line.
[d] Equivalent width of a line.
[e] The decrease in χ^2 when the Gaussian emission line is added to a simple power-law function.
[f] Fitting was performed over 2.5–15 keV owing to low photon statistics.

observations reported by Yaqoob & Serlemitsos (2000), and also adds new evidence from other observations in 1996–97.

It would be of interest to search for correlations between the presence of the line and the 3C 273 flux; however, the data available do not allow us to perform a convincing analysis of the line variability or of its relationship with the continuum variations. A future study along these lines will be very important for understanding where the cold matter emitting the fluorescence line is located with respect to the primary source.

4.3 Multifrequency spectrum

In order to understand the origin of hard X-ray emission from 3C 273 in more detail, we constructed a νL_ν multifrequency spectrum, adding our new *RXTE* results. The resultant multifrequency spectrum in the rest frame of the quasar ($z = 0.158$) is shown in Fig. 8. Crosses show *RXTE* data when the source was in the brightest state (MJD 50400.82–50400.83), whereas the filled circles show the data for the faintest state (MJD 50621.67–50621.69). Open circles and squares are archival data from the literature: NED data base (radio to ultraviolet), *ROSAT* (soft X-ray: Staubert 1992), OSSE, COMPTEL and EGRET on board *CGRO* (γ-rays: von Montigny et al. 1993, 1997). Three different peaks are apparent in the spectra: at low energies (LE: radio to optical) and high energies (HE: X-rays to γ-rays), with the BBB (optical to soft X-ray) in between.

To estimate the peak frequencies and luminosities of each component quantitatively, we fitted the spectral energy distribution (SED) with separate polynomial functions of the form $\log(\nu L_\nu) = a + b \log \nu + c\,(\log\nu)^2$, where a, b and c are constants. Similar polynominal fits were applied by Comastri, Molendi & Ghisellini (1995) for various blazars assuming cubic functions. In the case of 3C 273, however, there are only negligible differences between the quadratic and cubic functions, and hence we adopt the simpler quadratic form in the fitting. The results of quadratic fits are summarized in Table 4, where $L_{\rm p}$ is the *peak* luminosity in the νL_ν space, and $L_{\rm tot}$ is the *integrated* luminosity over that frequency range.

It must be noted that the most of the data in Fig. 8 were not obtained simultaneously. It is clear from a number of observations conducted at various times and at various wavelengths that 3C 273 is variable from radio to γ-ray energies (see von Montigny et al. 1997; Courvoisier 1998). Even for this particularly well-sampled and bright object, it has not yet been possible to obtain an actual 'snapshot' covering the total energy bandpass. Fortunately, the 30-yr monitoring of 3C 273 reveals that the variability amplitude is a factor of 4 at most energy bands (Türler et al. 1999). This is relatively small when plotted in the log ν–log(νL_ν) plane, and we thus believe that our discussion below is not affected significantly by the non-simultaneity of the data. We will comment on the effect of changes in physical parameters in Section 5.3.

5 DISCUSSION

5.1 Time variability

In Section 3, we have estimated the X-ray variability time-scale of 3C 273 using two different methods. We found that a roll-over appears at a time-scale of $t_{\rm var} \sim 3$ d, which is similar to the X-ray variability time-scale of Mrk 421 ($t_{\rm var} \sim 1$ d: Fig. 4). However, a clear difference was found in the *amplitude* of the variability (normalization in Fig. 4). In fact, the X-ray flux of Mrk 421 sometimes

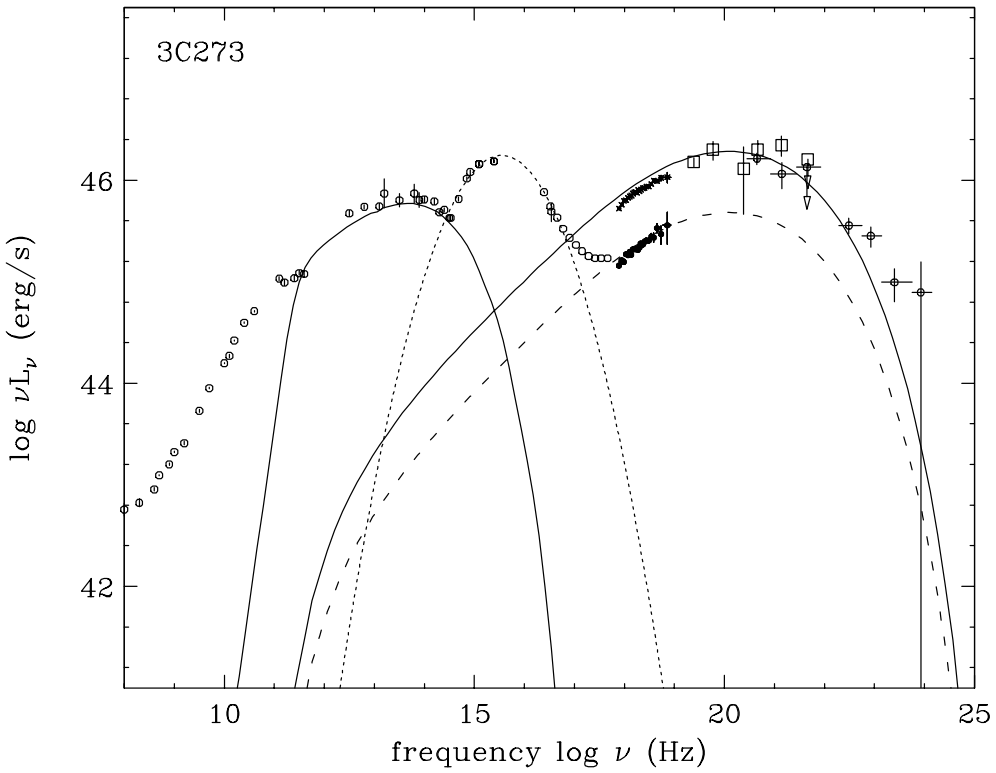

Figure 8. The multifrequency spectra of 3C 273. Open circles and squares: archival data from the literature. Crosses: *RXTE* data when the source was brightest, MJD 50400.8 (this work). Filled circles: *RXTE* data when the source was faintest, MJD 50621.7 (this work). The solid line shows the SSC model for parameters $B = 0.4$ G, $\delta = 10$, $\gamma_{\max} = 2000$ and $R = 2.5 \times 10^{16}$ cm. The dashed line shows a model for parameters $B = 0.4$ G, $\delta = 10$, $\gamma_{\max} = 2000$ and $R = 5.0 \times 10^{16}$ cm with moderate electron number density. All parameters are determined self-consistently as discussed in the text. The dotted line shows a quadratic fit to the BBB to guide the eye.

Table 4. Quadratic fit results of the 3C 273 SED.

Components	$\nu_{\rm p}$ (Hz)	$L_{\rm p}$ (erg s^{-1})	$L_{\rm tot}$ (erg s^{-1})
LE	$10^{13.5}$	$10^{45.8}$	$10^{46.7}$
HE[a]	$10^{20.0}$	$10^{46.2}$	$10^{47.1}$
BBB	$10^{15.5}$	$10^{46.2}$	$10^{46.8}$

[a]X-ray data taken during the brightest state are used for the fitting (MJD 50400.8; crosses in Fig. 8).

changes by more than a factor of 2 in a day (e.g. Takahashi et al. 2000), whereas flux variations of only 20–30 per cent are detected for 3C 273 (Fig. 2). Two possibilities may be considered to account for such a difference in variabilities.

We first assume 3C 273 to be a 'pure' blazar, i.e. most of the X-rays originate in beamed jet emission. Such an assumption may be valid since most of the time the X-ray photon spectra are well represented by a power-law function similar to other blazar-type objects. As many authors have suggested, variability in blazars may occur in a variety of ways, e.g. changes in the acceleration rate of electrons, magnetic field strength and/or beaming factor. The most convincing scenario that may reproduce the observation well is that electrons are accelerated to higher energy than usual during the flare (e.g. Mastichiadis & Kirk 1997; Kataoka et al. 2000). If this is the case, the different variability amplitudes may result from different physical processes for the X-ray production.

As expected from the multifrequency spectra, the X-ray photons are thought to be emitted from the *highest* energy electrons via the synchrotron process for Mrk 421 (Takahashi et al. 2000), whereas inverse Compton emission from the *low-energy* electrons is responsible for the case of 3C 273 (see Fig. 8). Since the higher energy electrons cool faster [$t_{\rm cool} \propto \gamma^{-1}$, where γ is the Lorentz factor of electrons (Rybicki & Lightman 1979)], it is a natural consequence that both the temporal and spectral evolutions are most pronounced at the highest end of electron population, as observed in Mrk 421. This scenario may well explain the apparent difference of variability amplitudes in Mrk 421 and 3C 273.

Alternatively, we next assume that 3C 273 is 'half-Seyfert/half-blazar'. It is clear that at some epochs at least, the X-ray flux has components that are *not* related to the beamed jet emission and which are observed to have fluxes similar to those discussed. This is particularly true of the soft excess and the broad-line feature discussed in Section 4.2. Thus we may have observed a combination of non-thermal X-ray emission from the beamed jet, and the isotropic thermal emission from the accretion disc at the same time. The two types of emission cannot be discriminated only from the X-ray data; however, variability in the lower energy band, in particular the BBB, provides an important hint.

The variability of the soft excess has been monitored for a long time. For example, Paltani et al. (1998) reported both optical and ultraviolet observations of 3C 273 covering the lifetime of the *IUE* satellite. They investigated the variability time-scales of the BBB using a structure function analysis. While the resulting SFs are characterized by a steep increase as for the X-ray band ($\beta \sim 1.5$: Fig. 4), a plateau appeared at much *longer* time-scale [$\tau \sim 0.5$ yr: but see Courvoisier et al. (1988) for an exceptionally rapid flare in the optical band].

If $\tau \sim 0.5$ yr were a 'typical' variability time-scale of the non-beamed isotropic component in 3C 273, this would produce a 'quasi-steady' underlying component to the 'rapidly variable' beamed jet emission. Such an offset may significantly reduce the amplitude of X-ray variability originating in the jet, but the observed time-scales (i.e. duration of a flare) would not be changed ($\tau \sim 3$ d). From this viewpoint, the difference of the variability amplitude in Mrk 421 and 3C 273 may be explained by the importance of underlying isotropic component over the beamed jet emission.

5.2 Spectral evolution

In Section 4, we showed that most 3C 273 photon spectra observed between 1996 and 2000 can be represented by a simple power-law function with $\Gamma = 1.6 \pm 0.1$. This is consistent with previously published results. Turner et al. (1990) suggest that the spectral index of 3C 273 in the 2–10 keV band is slightly harder than the "canonical' AGN index of $\Gamma = 1.7$, although the difference seems to be very small (1.5 compared with 1.7). Such a difference, if confirmed, may be due to a different physical origin of X-ray production.

In fact, X-ray photons are thought to be emitted from the Compton scattering of disc photons for Seyfert-type AGNs, whereas accelerated electrons in the jet produce non-thermal emission in the case of blazars. In the standard shock scenario (Fermi acceleration), electrons have a population $N(\gamma) \propto \gamma^{-2}$, where $N(\gamma)$ is the number density of electrons per unit energy. Such accelerated electrons emit photons with a spectrum of the form $\propto \nu^{-1.5}$, through both the synchrotron and inverse Compton processes (e.g. Rybicki & Lightman 1979). This is very close to the observational results.

If the hard X-ray photon index reflects the power-law index of the accelerated electrons (s of γ^{-s}), only small spectral changes would be expected in the photon spectra corresponding to the low-energy end of the electron populations (as for the X-ray photons of 3C 273). This is because low-energy electrons do not cool before leaving the emitting region, and hence keep their 'original' (injected) spectral information. As suggested by Kirk, Rieger & Mastichiadis (1998), changes in the electron injection rate could produce flux variations, but the photon spectra do not evolve significantly [$\propto \nu^{-(s+1)/2}$]. Such a scenario may well explain the spectral evolution observed in the 1996–97 season, where the photon index stays almost constant ($\Gamma \simeq 1.6$) regardless of the source flux variations.

In 1999–2000, a different spectral evolution was found, with the spectra becoming steeper (up to $\Gamma \sim 1.8$) as the source becomes brighter. This may be related to the *underlying* isotropic component emitted from the accretion disc or corona, as we have discussed in Section 5.1. It is interesting to note that the exceptional 'concave' photon spectrum was found only in this season (Fig. 7, left-hand panel). Such excess emission may be the hard tail of the BBB, as suggested from a *ROSAT* observation. Staubert (1992) reported a very steep X-ray spectrum of $\Gamma_{\rm L} \sim 2.6$ in the *ROSAT* bandpass (see also Fig. 8), which is marginally consistent with our results ($\Gamma_{\rm L} = 2.3 \pm 0.2$; Table 2). It is still unclear if the excess emission is really the hard tail of the BBB, as this feature was only clearly observed once, and *RXTE* has relatively poor sensitivity in the soft X-ray band. However, it seems plausible that non-beamed, thermal emission and its reprocessed flux become more important in the 1999–2000 season, compared with those in 1996–98: future studies are necessary to confirm this.

The broad-line feature is probably the Fe fluorescent line, as already discussed by Turner et al. (1990 *EXOSAT* and Ginga), Cappi et al. (1998 *ASCA*) and Yaqoob & Serlemitsos (2000 *ASCA* and *RXTE*). Interestingly, the Fe line is usually not visible in the *RXTE* observations; only nine of 261 observations clearly show line features, which is at odds with any thought that the hard X-ray photons are emitted by the same process as those in Seyfert galaxies. This suggests again that the X-ray photons of 3C 273 are *ordinarily* emitted from the relativistic jet, but that *occasionally* the emission from the accretion disc is visible (although it should be kept in mind that the *RXTE* PCA has a relatively low sensitivity for the broad-line feature, and that observations with a more sensitive spectrometer may have detected the line more frequently). The visibility of the Fe fluorescent line may depend on the balance between the jet emission, blue bump, and/or Compton scattering of disc photons. Future studies along these lines may be able to discriminate between various models of disc/jet connection.

In summary, we conclude that the hard X-ray emission of 3C 273 may occasionally contain a significant contribution from the accretion disc, but most hard X-rays are likely to originate in inverse Compton radiation from the relativistic jet.

5.3 Multifrequency spectrum

Multifrequency spectra provide information on physical quantities relevant for jet emission, e.g. the magnetic field, the size of the emission region, the maximum energy and the density of relativistic electrons. Various authors have determined jet parameters in a self-consistent manner for blazars (e.g. Mastichiadis & Kirk 1997; Kataoka et al. 2000; Kino, Takahara & Kusunose 2002), but only a few attempts have been made for 3C 273. We note again that part of the emission from 3C 273 may *not* be related to the beamed emission as discussed above. Nevertheless, we will consider this object as a 'blazar', for the following reasons.

(1) In contrast to many Seyfert galaxies (e.g. Mushotzky, Done & Pounds 1993), there is no hint of a 'reflection hump' corresponding to the Compton reflection of the primary component.

(2) Although some exceptions have been found, the X-ray photon spectra are generally well represented by a power-law function which smoothly connects to the γ-ray bands, as for other blazar-type objects.

von Montigny et al. (1997) examined three models to reproduce the multifrequency spectrum of 3C 273: (i) the synchrotron self-Compton model (SSC model: e.g. Inoue & Takahara 1996); (ii) the external radiation Compton model (ERC model: e.g. Sikora, Begelman & Rees 1994); and (iii) the proton-induced cascade model (PIC model: e.g. Mannheim & Biermann 1992). Although 3C 273 is one of the best-sampled and best-studied objects across the entire electromagnetic spectrum, they concluded that the data were still insufficient to discriminate between these models.

In the following, we thus adopt the simple one-zone SSC model to describe the spectrum. The resultant physical quantities provide a lot of feedback to test the validity of our assumptions. We will also comment on the applicability of other emission models, especially the ERC model, in the appendix. We do not consider the PIC model, in which the jet is composed of e^-–p plasma (baryonic) rather than e^-–e^+ plasma (leptonic). Such a situation might be possible, but observationally there are no reasons for considering additional, baryonic emission to account for the overall spectra [see Sikora & Madejski (2001) for a detailed discussion].

The jet parameters are tightly connected with the observed quantities, particularly the $\nu_{\rm p}$ and $L_{\rm tot}$ of each emission component (see Section 4.3). In the simple model that we adopt here, the radiation is due to a homogeneous jet component moving with a bulk

Lorentz factor $\Gamma_{\rm BLK}=(1-\beta^2)^{-1/2}$ at an angle to the line of sight of $\theta\simeq 1/\Gamma_{\rm BLK}$.

We first assume that the peak emissions ($L_{\rm p}$) of the low-energy (LE) synchrotron component and the high-energy (HE) inverse Compton (SSC) components arise from the *same* electron population with a Lorentz factor $\gamma_{\rm p}$. The peak frequencies of LE and HE are related by

$$\nu_{\rm HE,p}=\frac{4}{3}\gamma_{\rm p}^2\nu_{\rm LE,p}, \tag{3}$$

where $\nu_{\rm LE,p}=10^{13.5}$ Hz and $\nu_{\rm HE,p}=10^{20.0}$ Hz, respectively (Table 4). We thus obtain $\gamma_{\rm p}=2.0\times10^3$. The synchrotron peak frequency, $\nu_{\rm LE,p}$, is given by

$$\nu_{\rm LE,p}\simeq 3.7\times10^6 B\gamma_{\rm p}^2\frac{\delta}{1+z}\,{\rm Hz}, \tag{4}$$

where B is the magnetic field strength and $\delta=\Gamma_{\rm BLK}^{-1}(1-\beta\cos\theta)^{-1}\simeq\Gamma_{\rm BLK}$ is the relativistic beaming (Doppler) factor. The magnetic field B and its field densities are thus derived:

$$B=0.4\times\left(\frac{10}{\delta}\right){\rm G},\ U_B=6.7\times10^{-3}\left(\frac{10}{\delta}\right)^2{\rm erg\,cm^{-3}}. \tag{5}$$

Note that VLBI observations of 3C 273 set a lower limit for the Lorentz factor of $\Gamma_{\rm BLK}\geqslant 10$, implying that $\delta\sim\Gamma_{\rm BLK}\sim10$ if the angle to the line of sight of $\theta\simeq1/\Gamma_{\rm BLK}$ (e.g. Pearson et al. 1981; Krichbaum et al. 2002).

The ratio of the synchrotron luminosity, $L_{\rm LE,tot}$, to the inverse Compton (SSC) luminosity, $L_{\rm HE,tot}$, is

$$\frac{L_{\rm HE,tot}}{L_{\rm LE,tot}}=\frac{U_{\rm sync}}{U_B}, \tag{6}$$

where $U_{\rm sync}$ is the synchrotron photon energy density in the comoving frame of the jet. Using the observed value of $L_{\rm HE,tot}=10^{47.1}$ erg s^{-1} and $L_{\rm LE,tot}=10^{46.7}$ erg s^{-1} (Table 4), we obtain

$$U_{\rm sync}=2.0\times10^{-2}\left(\frac{10}{\delta}\right)^2{\rm erg\,cm^{-3}}. \tag{7}$$

Assuming a spherical geometry for the emission region, the synchrotron luminosity is given as

$$L_{\rm LE,tot}=4\pi R^2c\delta^4U_{\rm sync}\,{\rm erg\,s^{-1}}, \tag{8}$$

where R is the radius of the emission region. This radius is estimated as

$$R=2.5\times10^{16}\left(\frac{10}{\delta}\right){\rm cm}. \tag{9}$$

Remarkably, the size of the region derived here corresponds to the variability time-scale of $t_{\rm var}\simeq R/(c\delta)\simeq1$ d, qualitatively consistent with those expected from the temporal studies in Section 3. Also, if the jet is collimated within a cone of constant opening angle $\theta\simeq1/\Gamma_{\rm BLK}$, and the line-of-sight extent of the shock is comparable to the angular extent of the jet, one expects that the X-ray emission site is located at distance $D\sim10^{17-18}$ cm from the base of the jet. This implies that the radiation discussed here is emitted from the innermost part of the jet, i.e. 'sub-parsec-scale' jet. (This must be clearly distinguished from the 'large-scale' jet described later in this section.)

The SSC spectrum is *self-consistently* calculated assuming the parameters derived above. We assume an electron population of the form $N(\gamma)\propto\gamma^{-s}\exp(-\gamma/\gamma_{\rm p})$, where s is set to be 2. The solid line in Fig. 8 shows the overall model for the parameters $R=2.5\times10^{16}$ cm, $B=0.4$ G, $\delta=10$ and $\gamma_{\rm p}=2.0\times10^3$, while the dashed line shows the case when the region is larger by a factor of 2 with moderate electron number density (and other parameters unchanged). The whole spectrum is adequately represented, except for the discrepancy in the radio band. Such discrepancies are common for one-zone model fitting of blazar SEDs, as one-zone models cannot account for the low-energy emission, which is thought to be produced in a much larger region of the source (e.g. Marscher 1980).

The electron energy density, $U_{\rm e}$, is calculated to be 6.3×10^{-1} erg cm^{-3}, where we set the minimum energy of electrons to be $\gamma_{\rm min}=1$. The kinetic power of the electrons that emit the observed photons is thus estimated to be

$$L_{\rm kin}\simeq\pi R^2c\Gamma_{\rm BLK}^2U_{\rm e}\simeq3.7\times10^{45}\left(\frac{\delta}{10}\right)^2{\rm erg\,s^{-1}}. \tag{10}$$

It is interesting to compare these radiative/kinetic luminosities to discuss the 'power balance' between the accretion disc and the jet [see also Celotti, Padovani & Ghisellini (1997) and Celotti, Ghisellini & Chiaberge (2001) for the theoretical approach]. Assuming that the BBB is emitted isotropically from the accretion disc, the electromagnetic luminosity in the accretion disc is $L_{\rm disc}\simeq L_{\rm BBB,tot}=10^{46.8}$ erg s^{-1} (Table 4). The 'radiative power' and 'Poynting power' of the jet in the observer's frame are given as

$$L_{\rm rad}\simeq\pi R^2c\Gamma_{\rm BLK}^2U_{\rm ph}\simeq5.0\times10^{44}\left(\frac{10}{\delta}\right)^2{\rm erg\,s^{-1}}, \tag{11}$$

$$L_B\simeq\pi R^2c\Gamma_{\rm BLK}^2U_B\simeq3.9\times10^{43}\left(\frac{10}{\delta}\right)^2{\rm erg\,s^{-1}}, \tag{12}$$

respectively, where $U_{\rm ph}$ is the photon energy density in the jet comoving frame: $U_{\rm ph}\simeq U_{\rm sync}+U_{\rm SSC}$. By comparing $L_{\rm disc}$, $L_{\rm rad}$, L_B and $L_{\rm kin}$, we derive the following properties of the 'power balance' in the sub-parsec-scale jet:

(1) the kinetic power of *relativistic* electrons amounts to only 5–10 per cent of the BBB emission, which is thought to be radiated in the vicinity of the central black hole;

(2) the magnitudes of the powers are $L_{\rm kin}\geqslant L_{\rm rad}\geqslant L_B$.

We finally comment on the large-scale X-ray jet observed by *Einstein* (Harris & Stern 1987), *ROSAT* (Röser et al. 2000) and *Chandra* (Sambruna et al. 2001; Marshall et al. 2001). The X-ray jet is ~8 arcsec (1 arcsec = 2.4 kpc at the distance of 3C 273) long and has a knotty morphology, starting with a bright, resolved knot ~13 arcsec from the core. This 'kpc-scale jet' is much fainter than the 'sub-parsec-scale jet'. Indeed, the integrated X-ray flux of the kpc-scale jet is 6.9 ± 0.6 nJy at 1 keV (Marshall et al. 2001), which corresponds to ~0.1 per cent of the X-ray flux emitted from the 'sub-parsec-scale jet'. The spectral energy distributions from radio to X-rays of the individual knots show a variety of shapes. Sambruna et al. (2001) fit the multifrequency data of each knot with the ERC/CMB model, where the cosmic microwave background (CMB) photons are up-scattered into the X-ray band. For example, they obtain the best-fitting parameters for region A (see Sambruna et al. 2001 for definition) of electron index $s=2.6$, normalization $K=8.1\times10^{-3}$ cm^{-3}, magnetic field $B=1.9\times10^{-6}$ G, region size $R=5\times10^{21}$ cm and Doppler factor $\delta=5.2$.

Assuming these quantities, we estimate the kinetic power in the 10-kpc-scale jet as $L_{\rm kin,10\,kpc}=10^{47.1}(20/\gamma_{\rm min})^{0.6}$ erg s^{-1}, which is about 2 orders of magnitude larger than that in the sub-parsec-scale jet discussed above [$L_{\rm kin,sub\text{-}pc}\sim4\times10^{45}$ erg s^{-1}; see equation (10)]. It should be noted that the kinetic power of electrons strongly depends on both the minimum energy ($\gamma_{\rm min}$) and the power-law index

(s) of the assumed electron population. Part of the difference may be explained by different parameters selected above; however, it seems difficult to explain the discrepancy completely by this fact alone. In fact, if we assume $\gamma_{\rm min} = 1$ for the 10-kpc-scale jet, as was assumed for the sub-parsec-scale jet, $L_{\rm kin,10\,kpc}$ becomes *larger*, increasing the discrepancy. Similarly, an electron population with $s = 2.0$ would minimize $L_{\rm kin,10\,kpc}$, but such parameters would not fit the observed SED so well. Future observations of the 10-kpc-scale jet with wider energy bands are eagerly awaited.

If the difference between the sub-parsec- and the 10-kpc-scale jet powers is confirmed, this may imply that $\sim$100 times the 'visible' kinetic energy is *hidden* at the bottom of the jet. It should be noted that the kinetic power discussed above takes account of only *relativistic* electrons; in other words, the contribution from thermal electrons as well as protons (either relativistic or cold) has been completely neglected. These non-relativistic electrons and/or protons cannot contribute to the emission in the sub-parsec-scale jet.

Only a small fraction of them, probably less than 1 per cent in number, may be 'picked up' by the shock acceleration process, to add to the relativistic electron population. Such a low acceleration efficiency may well be understood by the so-called *internal* shock model as discussed by Spada et al. (2001) and Kataoka et al. (2001). Further investigations along these lines are now in progress. For example, Tanihata (2002) suggests that, in order to explain the observed variability properties, the velocity difference of the two colliding shells must be rather small. For this case, the efficiency is estimated to be as small as $\leqslant$0.01 per cent.

The enormous kinetic energy could be released for the first time at large distances (e.g. $\geqslant$10 kpc) by completely different mechanisms of energy dissipation. One such possibility is the *external* shock model, wherein shocks arise when outflowing jet plasma decelerates upon interaction with dense gas clouds originating outside the jet (e.g. Dermer & Chiang 1998). The precise nature of the required gas clouds is uncertain, but shock acceleration takes place more efficiently than for the *internal* shock model. Meanwhile, the different jet powers may imply that part of the kinetic power carried by *protons* in the sub-parsec-scale jet is efficiently transferred to the *electrons* in the 10-kpc-scale jet, although the mechanisms of energy dissipation are completely uncertain. Future deep observations of large-scale jets by *Chandra* and *Newton* may be able to confirm our suggestions about the power consumption in the 3C 273 jet.

6 CONCLUSION

We have analysed the archival *RXTE* data available for 3C 273 between 1996 and 2000. A total of 230 observations amounts to a net exposure of 845 ks over the 4 years. This is the longest, and most densely sampled, exposure for this object in the hard X-ray band. Both the PSD and the SF show a roll-over with a time-scale of the order of $\sim$3 d, although the lower frequency (i.e. longer time-scale) variability is still unclear. We found that the variability time-scale of 3C 273 is similar to those observed in TeV γ-ray-emitting blazars, whereas the variability amplitude is an order of magnitude smaller. Considering that the hard X-ray spectra of 3C 273 generally maintain a constant power-law shape with $\Gamma \simeq 1.6 \pm 0.1$, beamed, inverse Compton emission inside the jet is the most likely the origin of the X-ray/γ-ray emission. Two kinds of exceptions have been found, which may be interpreted as either the hard tail of the BBB or emission from the accretion disc *occasionally* superposed on the jet emission. From a multifrequency analysis, we constrain the physical quantities relevant for the jet emission. We argue that (i) the kinetic power carried by *relativistic* electrons corresponds to only 5–10 per cent of the disc luminosity, and (ii) the various powers in the sub-parsec-scale jet are ranked $L_{\rm kin} \geqslant L_{\rm rad} \geqslant L_B$. The connection between the sub-parsec-scale jet and the 10-kpc-scale jet remains uncertain, but our work suggests that the most of the jet power might be *hidden* at the base of the sub-parsec-scale jet, and effectively released at the 10-kpc scale via a completely different mechanism of energy dissipation.

ACKNOWLEDGMENTS

We greatly appreciate the referee, Dr J. T. Courvoisier, for his helpful comments and suggestions to improve the manuscript. This research has made use of the NASA/IPAC Extragalactic Data base (NED), which is operated by the Jet Propulsion Laboratory, California Institute of Technology, under contract with the National Aeronautics and Space Administration.

REFERENCES

Abraham Z., 2000, A&A, 355, 915
Cagnoni I., Papadakis I. E., Fruscione A., 2001, ApJ, 546, 886
Cappi M., Matsuoka M., Otani C., Leighly K. M., 1998, PASJ, 50, 213
Celotti A., Padovani P., Ghisellini G., 1997, MNRAS, 286, 415
Celotti A., Ghisellini G., Chiaberge M., 2001, MNRAS, 321, L1
Comastri A., Molendi S., Ghisellini G., 1995, MNRAS, 277, 297
Courvoisier T. J.-L., 1998, A&AR, 9, 1
Courvoisier T. J.-L., Clavel J., 1991, A&A, 248, 389
Courvoisier T. J.-L., Robson E. I., Hughes D. H., Blecha A., Bouchet P., 1988, Nat, 335, 330
Czerny B., 1994, in Courvoisier T. J. L., Blecha A., eds, Proc. IAU Symp. 159, Multi-wavelength continuum emission of AGN. Kluwer, Dordrecht, p. 261
Dermer C. D., Chiang J., 1998, New Astron., 3, 157
Dermer C. D., Schlickeiser R., 1993, ApJ, 416, 458
Dickey J. M., Lockman F. J., 1990, ARA&A, 28, 215
Ghisellini G., Celotti A., Fossati G., Maraschi L., Comastri A., 1998, MNRAS, 301, 451
Grandi P. et al., 1997, A&A, 325, L17
Haardt F. et al., 1998, A&A, 340, 35
Harris D. E., Stern C. P., 1987, ApJ, 313, 136
Hartman R. C. et al., 1999, ApJS, 123, 79
Hayashida K., Miyamoto S., Negoro H., Inoue H., 1998, ApJ, 500, 642
Hughes P. A., Aller H. D., Aller M. F., 1992, ApJ, 396, 469
Inoue S., Takahara F., 1996, ApJ, 463, 555
Jahoda K. et al., 1996, in Proc. SPIE Vol. 2808, EUV, X-ray and Gamma-ray Instrumentation for Astronomy VII. SPIE, Bellingham, p. 59
Kataoka J., Takahashi T., Makino F., Inoue S., Madejski G. M., Tashiro M., Urry C. M., Kubo H., 2000, ApJ, 528, 243
Kataoka J. et al., 2001, ApJ, 560, 659
Kino M., Takahara F., Kusunose M., 2002, ApJ, 564, 97
Kirk J. G., Rieger F. M., Mastichiadis A., 1998, A&A, 333, 452
Krichbaum T. P. et al., 2002, in Laing R. A., Blundell K. M., eds, ASP Conf. Ser. Vol. 250. Astron. Soc. Pac., San Francisco, in press
M$^{\rm c}$Hardy I., Newsam A., Marscher A., Robson I., Stevens J., 1999, MNRAS, 310, 571
McNaron-Brown K. et al., 1995, ApJ, 451, 575
Mannheim K., Biermann P. L., 1992, A&A, 253, L21
Marscher A. P., 1980, ApJ, 235, 386
Marshall H. L. et al., 2001, ApJ, 549, L167
Mastichiadis A., Kirk J. G., 1997, A&A, 320, 19
Mukherjee R. et al., 1997, ApJ, 490, 116
Mushotzky R. F., Done C., Pounds K. A., 1993, ARA&A, 31, 717
Ohashi T. et al., 1996, PASJ, 48, 157
Paltani S., Courvoisier T. J.-L., Blecha A., Bratschi P., 1997, A&A, 327, 539
Paltani S., Courvoisier T. J.-L., Walter R., 1998, A&A, 340, 47

Pearson T. J., Unwin S. C., Cohen M. H., Linfield R. P., Readhead A. C. S., Seielstad G. A., Simon R. S., Walker R. C., 1981, Nat, 290, 365
Rieger F. M., Mannheim K., 2000, A&A, 359, 948
Robson I., 1996, in Active Galactic Nuclei. Wiley, New York
Röser H.-J., Meisenheimer K., Neumann M., Conway R. G., Perley R. A., 2000, A&A, 360, 99
Rybicki G. B., Lightman A. P., 1979, in Radiative Processes in Astrophysics. Wiley New York
Sambruna R. M., Urry C. M., Tavecchio F., Maraschi L., Scarpa R., Chartas G., Muxlow T., 2001, ApJ, 549, L161
Schönfelder V. et al., 2000, A&AS, 143, 145
Shields G. A., 1978, Nat, 272, 706
Sikora M., Madejski G., 2001, in Aharonian F., Völk H., eds, AIP Conf. Ser. Vol. 558, Int. Symp. on High Energy Gamma-Ray Astronomy. Am. Inst. Phys., New York, p. 275
Sikora M., Begelman M. C., Rees M. J., 1994, ApJ, 421, 153
Simonetti J. H., Cordes J. M., Heeschen D. S., 1985, ApJ, 296, 46
Spada M., Ghisellini G., Lazzati D., Celotti A., 2001, MNRAS, 325, 1559
Staubert R., 1992, MPE Rep., 235, 42
Swanenburg B. N. et al., 1978, Nat, 275, 298
Takahashi T. et al., 2000, ApJ, 542, L105
Tanihata C., 2002, PhD thesis, University of Tokyo
Türler M. et al., 1999, A&AS, 134, 89
Turner M. J. L. et al., 1990, MNRAS, 244, 310
Ulrich M.-H., Maraschi L., Urry C. M., 1997, ARA&A, 35, 445
Urry C. M., Padovani P., 1995, PASP, 715, 803
Vermeulen R. C., Cohen M. H., 1994, ApJ, 430, 467
von Montigny C. et al., 1993, A&AS, 97, 101
von Montigny C. et al., 1997, ApJ, 483, 161
Yamashita A. et al., 1997, IEEE Trans. Nucl. Sci., 44, 847
Yaqoob T., Serlemitsos P., 2000, ApJ, 544, L95
Yaqoob T. et al., 1994, PASJ, 46, L49

APPENDIX A: APPLICABILITY AND VALIDITY OF THE SSC/ERC MODELS

Finally, we comment on an alternative scenario which may account for the overall spectra of 3C 273, namely the external radiation Compton (ERC) model.

A number of quasars show complicated multifrequency spectra which cannot be readily fitted with a simple SSC model. This is mostly because the γ-ray flux strongly dominates the radiative output, and the γ-ray spectra are well above the extrapolation of the X-ray spectra (e.g. Ghisellini et al. 1998). One explanation is that the SSC process dominates in the X-ray range, while the ERC process dominates in γ-rays (e.g. Inoue & Takahara 1996). Such a discontinuity/complexity cannot be seen for 3C 273 in Fig. 8, suggesting that both the X-rays and γ-rays are produced by the *same* radiation process, i.e. the SSC process – that is the main reason why we apply the SSC model to the data in Section 5.3.

However, this explanation is unable to reject other emission models, in particular the ERC model. This is because most of the data are obtained non-simultaneously, and we do not have an actual 'snapshot' of the overall emission. In fact, the ERC model provides a similarly good fit for the case of 3C 273, as discussed in detail by von Montigny et al. (1997). In this appendix, we consider in what situation the SSC dominates the ERC process, and what the expected impact would be if the ERC model were responsible for the overall emission from 3C 273.

Within the framework of ERC models, a number of possibilities exist for the origin of the seed photons which are up-scattered to γ-rays. Dermer & Schlickeiser (1993) suggest that the direct emission from the central core irradiates the emission region inside the jet, which may provide a sufficient number of seed photons. In the observer's frame, the isotropic luminosity of the central core is approximated by

$$L_{\rm core} \simeq L_{\rm disc} \simeq L_{\rm BBB,tot} = 6.3 \times 10^{46}\,{\rm erg\,s^{-1}} \tag{A1}$$

(see Table 4). In the co-moving frame of a jet with bulk Lorentz factor $\Gamma_{\rm BLK}$, the photon energy density that is produced by the core emission is given as

$$U_{\rm ext,in} = \frac{L_{\rm core}}{4\pi d^2}\frac{\Gamma_{\rm BLK}^2(1+\beta^2-2\beta)}{c} \simeq \frac{L_{\rm core}}{4\pi d^2}\frac{1}{4\Gamma_{\rm BLK}^2 c}, \tag{A2}$$

where d is the distance from the central core. By normalizing by typical values of $\Gamma_{\rm BLK}$ and d, we obtain

$$U_{\rm ext,in} = 4.6 \times 10^{-3}\left(\frac{0.1{\rm pc}}{d}\right)^2\left(\frac{10}{\Gamma_{\rm BLK}}\right)^2 {\rm erg\,cm^{-3}}. \tag{A3}$$

Comparing this with the synchrotron photon energy density, $U_{\rm sync} = 2.0 \times 10^{-2}(10/\delta)^2$ erg cm^{-3} (see equation 7), direct emission from the central core cannot be a dominant source of seed photons for the ERC process. This is because the jet plasma is moving away from the central core at highly relativistic speed ($\Gamma_{\rm BLK} \simeq 10$), and hence is strongly *red*shifted as measured in the source co-moving frame.

The second candidate source of the external seed photons is the 'diffuse' radiation field, i.e. a radiation field having a significant non-radial component at large distance from the central engine. Such a radiation component may be produced by scattering or reprocessing of a portion of the central radiation by irradiated clouds and/or the inter-cloud medium (Sikora et al. 1994). Importantly, all photons directed inward toward the central source are *blue*shifted, and enhanced by a factor of $\Gamma_{\rm BLK}$ in the frame co-moving with the jet. Assuming that a certain fraction τ (<1) of the central luminosity is reprocessed into such a diffuse radiation field, we obtain

$$U_{\rm ext,out} = \frac{\tau L_{\rm core}}{4\pi d^2}\frac{\Gamma_{\rm BLK}^2}{c}. \tag{A4}$$

If the SSC process is more likely origin of the X-ray/γ-ray emissions, as we have assumed in Section 5.3, inverse Comptonization of external photons does *not* dominate the synchrotron photons and $U_{\rm sync} \geqslant U_{\rm ext,out}$ must hold. This limits the fraction τ very tightly to

$$\tau \leqslant 1.1 \times 10^{-4}\left(\frac{d}{0.1\,{\rm pc}}\right)^2\left(\frac{10}{\Gamma_{\rm BLK}}\right)^4, \tag{A5}$$

meaning that less than 0.01 per cent of the BBB luminosity could be reprocessed into the 'isotropic' external radiation field in the case of 3C 273. One difficulty in understanding the overall photon spectrum of 3C 273 with the SSC model is why such a low efficiency is achieved in this object – unfortunately, we still do not have an answer to this question.

One may therefore consider the *opposite* extreme, when the X-ray and γ-ray emissions are dominated by the ERC process, rather than SSC emission. In such a situation, the ratio of the synchrotron luminosity, $L_{\rm LE,tot}$, to the inverse Compton (ERC) luminosity, $L_{\rm HE,tot}$, is (see also equation 6)

$$\frac{L_{\rm HE,tot}}{L_{\rm LE,tot}} = \frac{U_{\rm ext,out}}{U_B}. \tag{A6}$$

The magnetic field density is estimated to be

$$U_B \simeq \frac{L_{\rm LE,tot}}{L_{\rm HE,tot}}\frac{\tau L_{\rm core}}{4\pi d^2}\frac{\Gamma_{\rm BLK}^2}{c}. \tag{A7}$$

The reprocessing factor τ is very uncertain, but it must be larger than 10^{-4} if the ERC process dominates (see equation A5). Normalizing

τ with 10^{-3}, and assuming the observed values of $L_{\rm LE,tot}$, $L_{\rm HE,tot}$ and $L_{\rm core} \simeq L_{\rm BBB,tot}$ (Table 4), we obtain

$$B \simeq 1.4 \times \left(\frac{\tau}{10^{-3}}\right)^{1/2} \left(\frac{\Gamma_{\rm BLK}}{10}\right) \left(\frac{0.1\,{\rm pc}}{d}\right) {\rm G}. \quad \text{(A8)}$$

Thus, in the framework of the ERC model, the overall emission of 3C 273 may be reproduced if the magnetic field strength is a bit stronger than in the SSC case.

In both the SSC and ERC models, the low-energy component is thought to be produced by the same synchrotron process. The synchrotron luminosity $L_{\rm LE,tot}$ behaves as

$$L_{\rm LE,tot} \propto U_B U_{\rm e} R^3. \quad \text{(A9)}$$

In order to explain the observed $L_{\rm LE,tot}$ with a *different* magnetic field strength B ($\simeq$0.4 G for the SSC and $\simeq$1.4 G for the ERC model), the electron energy density $U_{\rm e}$ must be varied since R is constrained to 10^{16-17} cm from the observed variability time-scale. Thus the $U_{\rm e}$ of the ERC model could be smaller by about an order of magnitude than we have assumed for the SSC model, $U_{\rm e} \sim 5 \times 10^{-2}$ erg cm^{-3}. This may lead to an overestimate of the kinetic power if the overall X-ray/γ-ray spectra are dominated by the ERC (see equation 10). However, what is important is that, assuming either the SSC or the ERC model, our discussion and conclusions about the power balance in the jet (see Section 5.3) are not affected significantly.

This paper has been typeset from a TEX/LATEX file prepared by the author.